Chiral Symmetry Breaking of Tight-Binding Models in Coupled Acoustic-Cavity Systems

Ze-Guo Chen,[1] Licheng Wang,[1,2] Guanqing Zhang,[1] and Guancong Ma[1,*]

[1] *Department of Physics, Hong Kong Baptist University, Kowloon Tong, Hong Kong*

[2] *Department of Applied Physics, Guangdong University of Technology, Guangzhou 510090, China*

(Received 31 March 2020; revised 2 July 2020; accepted 6 July 2020; published 11 August 2020)

A finite one-dimensional Su-Schrieffer-Heeger (SSH) chain exhibits "zero-energy" boundary-mode solutions that are protected by chiral symmetry. The breaking of chiral symmetry leads to several important consequences, including a shift of the boundary mode energies. Here, we systematically study the coupled acoustic-cavity system (CACS), which is an important acoustic platform for realizing tight-binding models (TBMs). We find that the length and number of coupling waveguides not only affect hopping, but also induce a perturbation to the onsite eigenfrequency, which can be attributed to the breaking of chiral symmetry in the TBM. The acoustic origin of these phenomena is discussed, and the conditions of the exact realization of TBMs are identified. Meanwhile, we build an acoustic second-order topological insulator by extending the SSH model to two dimensions and show that the frequency of the topological corner modes is tunable by the same chiral-symmetry-breaking term. This finding is experimentally validated through the demonstration of in-gap and in-band topological corner modes. Our study provides a detailed and accurate understanding of the CACS and clarifies several important nuances for realizing tight-binding systems in acoustics. These results solidify CACS as a foundation for future studies of topological acoustics and non-Hermitian acoustics.

DOI: 10.1103/PhysRevApplied.14.024023

I. INTRODUCTION

Topological phases of matters are underpinned by the consideration of the global properties of the eigenfunctions. These considerations are universal and have brought revolutions across many disciplines of physics [1–3]. As a scalar wave, sound is among the simplest forms of waves. Compared with electromagnetic waves and electrons, it lacks the spin degree of freedom and is inert to many interactions, such as the response to a magnetic field, which are regarded as fundamental to some topological phases. In spite of these disadvantages, acoustic wave systems have nevertheless emerged as a fertile ground for the study of the fascinating novel properties of topological phases of matter [4]. A rich variety of topological phases, including the acoustic Chern insulator [5–8], the valley Hall insulator [9], the pseudospin Hall insulator [10, 11], Weyl semimetals [12–14], and higher-order topological insulators [15–18], have been proposed and realized. The success of topological acoustics exemplifies the fundamental role of symmetry breaking in topological phases. The system's symmetry can often be encoded in a Hamiltonian with a mathematically simple form by using a tight-binding model (TBM). In addition, the TBM is also a foundation for the study of non-Hermitian physics [19–21]. In acoustics, the coupled acoustic-cavity system (CACS), due to its versatile tunability and ease of fabrication, is widely adapted for the realization of TBMs [22–30]. The widespread use of CACSs demands a systematic study, which is also beneficial in revealing its full potential.

Here, we investigate the CACS and its validity for realizing TBMs. We find that the CACS can ideally reproduce a TBM only with a specific set of geometric parameters that are determined by the ratio of the lengths of the coupling waveguide and the depth of the cavity. Away from these parameters, the coupling waveguides induce a perturbation to the system's onsite eigenfrequency. We show with a Su-Schrieffer-Heeger (SSH) model that this perturbation contributes to the breaking of chiral symmetry, which causes a drift in the frequency of zero-energy boundary modes. By further extending to two-dimensional (2D) SSH lattices, we demonstrate with experiments that the chiral-symmetry-breaking effect becomes a degree of freedom for tuning the spectral position of second-order topological corner modes relative to the bulk bands.

*phgcma@hkbu.edu.hk

II. ANALYSIS OF THE CACS

A. Precise realization of TBM using CACS

A CACS consists of an array of acoustic-cavity resonators, typically made of solid materials and filled with fluid, such as air. The cavities are connected by waveguides with subwavelength cross sections. As such, the resonant mode of the acoustic cavity plays the role of an onsite orbital, and the waveguides provide an interchange of energy among the cavities. We begin by considering a 2D two-cavity system, as shown in Fig. 1(a). Here, the cavity has a length L_0 and width D_0, where we set $L_0 \gg D_0$.

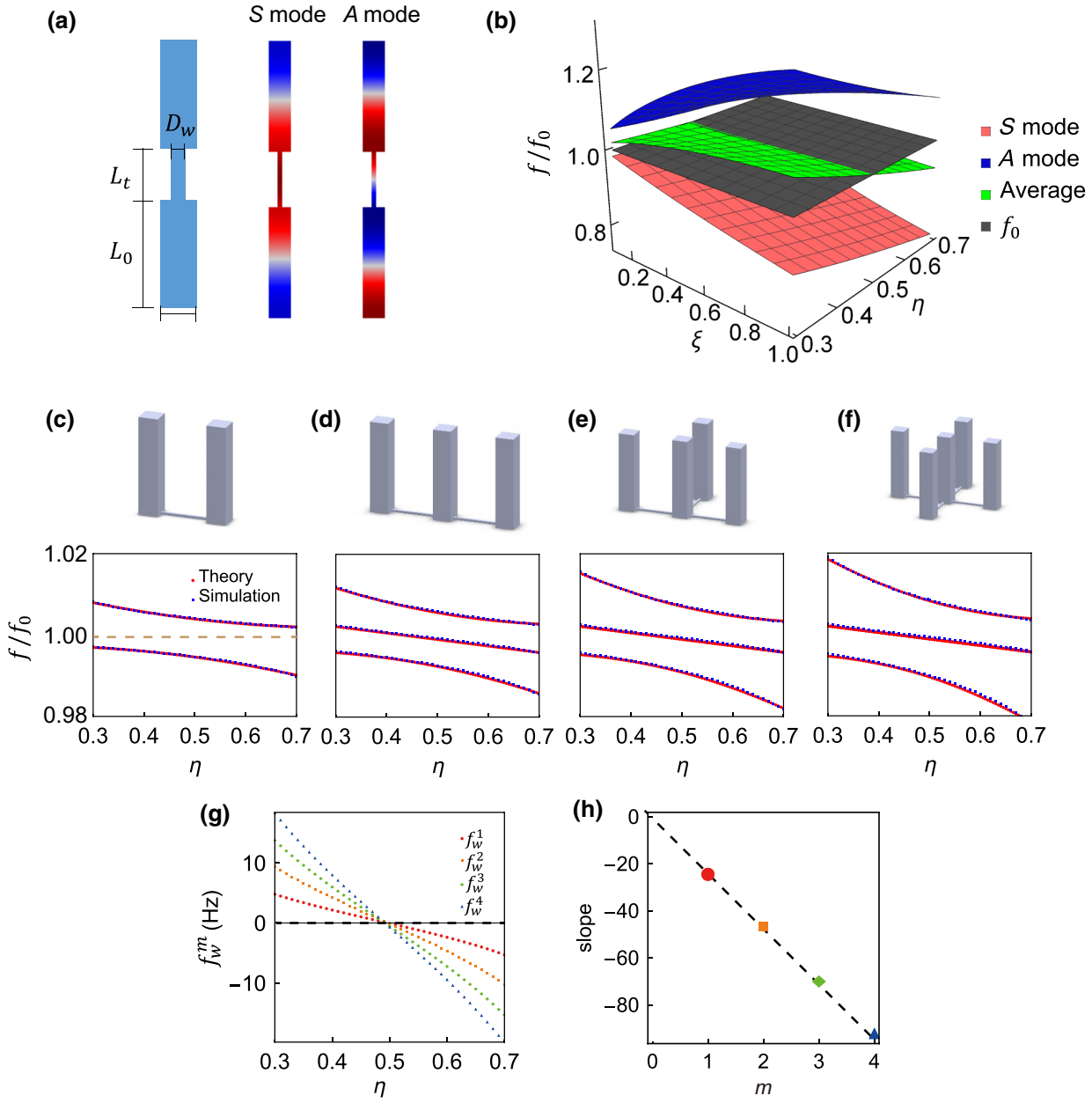

FIG. 1. (a) Schematic of a 2D CACS that can be described by a two-level TBM. Profiles of the coupled modes are shown, with red, blue, and white indicating negative, positive, and zero pressure, respectively. (b) Calculated eigenfrequencies of the system near the first resonant frequency, $f_0 = c/2L_0$, as functions of η and ξ. Frequency of the symmetric (antisymmetric) mode is plotted as the red (blue) surface. Average of the two is plotted in green. Gray plane represents f_0. Green and gray surfaces intersect at $\eta = 0.5$. Two (c), three (d), four (e), and five (f) coupled cavities. Eigenfrequencies of each system are plotted in the lower panels as functions of η. Blue dots are the results obtained from finite-element simulations and red dots are computed using the TBM [Eq. (3)]. (g) Onsite perturbations as functions of η. Number of coupling waveguides on one cavity also affects such perturbations. (h) Perturbations follow linear fits with slopes proportional to the number of waveguides m.

We choose the first cavity mode as the onsite orbital, with a resonant frequency $f_0 = c/2L_0$, where c is the speed of sound in the filling medium. The cavities are connected by a narrow waveguide, providing hopping t. The system can be modeled by a two-level Hamiltonian, $H = \begin{pmatrix} f_0 & t \\ t & f_0 \end{pmatrix}$, which has symmetric and antisymmetric modes [Fig. 1(a)]. It is well known that the magnitude of hopping t is tunable by the coupling waveguide's width [21,22].

Here, we consider the influence of length L_t of waveguides, which has not been explored in previous studies. The eigenfrequencies of the two-cavity system are functions of $\eta = L_t/L_0$ and $\xi = D_w/D_0$, i.e., the length and width ratios of the coupling waveguide and the cavity, as shown in Fig. 1(b). The symmetric and antisymmetric modes are represented by red and blue surfaces, respectively. Notably, the symmetric mode is at a lower frequency, indicating that t is negative. We also plot the average of the two eigenfrequencies as the green surface, and the gray plane is f_0. First, it is clear that the green and gray surfaces do not overlap, indicating a deviation of the averaged frequency from f_0. This implies that, in general, the CACS does not exactly realize an ideal TBM and that the coupling waveguides generally introduce an additional perturbation to onsite frequency.

Nevertheless, the green surface and gray plane intersect near $\eta = 0.5$, and the CACS can be regarded as an ideal TBM along the intersecting line [Fig. 1(b)]. To understand this condition, we note that an ideal TBM yields two coupled modes with opposite parity. To further elaborate, consider the extreme case of $\xi = 1$, i.e., when the system becomes one long uniform cavity with length $L_t + 2L_0 = L_t[1 + (2/\eta)]$, so the sum of the two neighboring eigenfrequencies must equal $2f_0$, i. e.,

$$\frac{nc}{2(L_t + 2L_0)} + \frac{(n+1)c}{2(L_t + 2L_0)} = \frac{c}{L_0}, \tag{1}$$

where n represents the nth eigenmode of the long uniform cavity with length $L_t + 2L_0$. Equation (1) yields

$$\eta = n - \frac{3}{2}. \tag{2}$$

Notably, the smallest positive value of η occurs when $n = 2$, which gives a minimum length of $L_t = 0.5L_0$. Meanwhile, since we are considering only cavity modes that have no variation in the transverse direction, the waveguide's width, D_w, has a negligible effect on the sum of the two eigenfrequencies, when D_w is much smaller than L_0. This is also seen for $\xi = 0$, at which the two cavities become isolated, each with onsite frequency f_0.

Figure 1(c) shows a realization of a 2D CACS using realistic acoustic cavities. Notably, the coupling waveguide and the cavities are perpendicular. However, their relative orientation does not significantly impact the result. Here, the coupling waveguide is much thinner than the height of the cavity, to take advantage of the near-uniform sound field near the ends of the cavities. The cavities have a height of $L_0 = 120$ mm and square cross section with a side length of $D_0 = 24$ mm. The simulation yields an onsite eigenfrequency of 1429 Hz. The coupling waveguide has a width $D_w = 3$ mm, which is much smaller than that of L_0. The lower panel of Fig. 1(c) plots the two coupling modes' eigenfrequencies as functions of η. We can indeed see the drift of the average frequency, which is aligned with our analysis based on the 2D model [Figs. 1(a) and 1(b)].

A cavity is often connected to multiple neighbors to form a lattice. Therefore, it is necessary to investigate the possible effects of the number of coupling waveguides on a single cavity. To do so, we examine several cases, as shown in Figs. 1(c)–1(f). The revised Hamiltonian can be written as

$$H_m = \sum\nolimits_i^{m+1} \{[f_0 + f_w^m(\xi,\eta)]c_i^\dagger c_i\} + \sum\nolimits_{i,j} [w(\xi,\eta)c_i^\dagger c_j + \text{H.c.}], \tag{3}$$

where i labels the sites, i and j label the cavities that are connected to the nearest neighbor by a waveguide(s); $c_i^\dagger$ and c_i are the creation and annihilation operators, respectively; $w(\xi,\eta)$ is the hopping coefficient of two connected cavities; and $f_w^m(\xi,\eta)$ is the frequency perturbation to the onsite frequencies by the waveguides, where the superscript m denotes the number of waveguides on a specific cavity. Based on Eq. (3), we plot the eigenfrequency spectra of the system with fixed $D_w = 3$ mm as functions of η in Figs. 1(c)–1(f). The results from our model agree well with the simulated results obtained using COMSOL Multiphysics. In Fig. 1(g), we plot the onsite perturbations f_w^m as functions of η. We find that the perturbations satisfy $f_w^m = mf_w^1 = -23.9m(\eta - 0.5)$ Hz, as shown in Fig. 1(h), indicating that the perturbations are linearly related to m, which is the number of connecting waveguides. This relation is essential when considering the boundary modes in SSH models, and when extending the model to 2D, which is discussed later.

B. Tuning the sign of hopping

On the other hand, the sign of hopping, w, is tunable via adjusting the length of the coupling waveguide. This can be seen as follows. The increase of η by increasing the waveguide length L_t, while keeping the cavity height L_0 constant, results in a higher waveguide mode of f_0. In the example shown in Fig. 2(a), when $\eta < 1$, the symmetric mode has no node inside the coupling waveguide and is below the antisymmetric mode. As η approaches one, the frequency of the symmetric mode drops drastically. When $\eta > 1$, however, a higher symmetric mode with two nodes inside the coupling waveguide appears near f_0. In

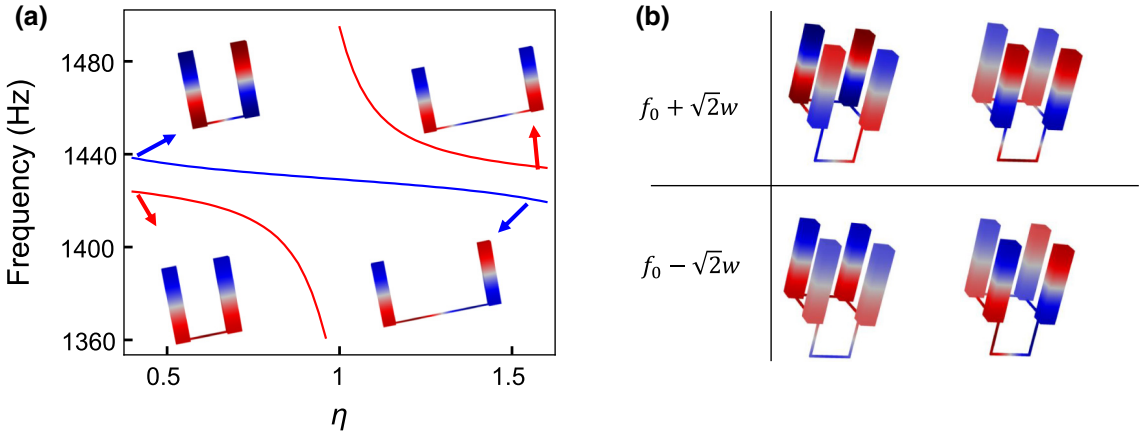

FIG. 2. Sign of hopping can be tuned in CACS by tuning the length of the coupling waveguide. (a) In a two-cavity system, symmetry types of the two modes near f_0 switch as η crosses unity. (b) Four-cavity system with three short coupling waveguides ($L_t = 0.5L_0$) and one long waveguide ($L_t = 1.5L_0$). Four eigenmodes are doubly degenerate at $f_0 \pm \sqrt{2}w$.

other words, when $\eta > 1$, the symmetric mode has a higher frequency than that of the antisymmetric mode. In the TBM, such a change in ordering of the eigenmodes can be represented as $[1, -\mathrm{sgn}(w)]$, which indicates a change in hopping at $\eta = 1$.

To further corroborate this point, we show another example that is composed of four cavities, each connected to its nearest neighbor. Here, three coupling waveguides have a length of $0.5L_0$ (i.e., $\eta = 1/2$), whereas the fourth waveguide's length is $1.5L_0$ ($\eta = 3/2$). The system's eigenmodes are doubly degenerate, with eigenfrequencies $f_0 \pm \sqrt{2}w$ [Fig. 2(b)]. According to the TBM, this can only be the consequence of one of the four hopping coefficients having an opposite sign.

These results confirm that the length of the coupling waveguides can tune the hopping sign in the system. Such a degree of freedom plays an essential role in constructing novel topological phases, such as topological quadruple [18,31] or octupole insulators [32].

III. CHIRAL SYMMETRY BREAKING IN ONE-DIMENSIONAL ACOUSTIC SSH MODEL

A one-dimensional (1D) periodic chain can be constructed by repeating the two-cavity system. As shown in Fig. 3(a), each cavity in the bulk is connected to its nearest neighbors by two waveguides with different side widths $D_w = 3\,\mathrm{mm}$ and $D_v = 9\,\mathrm{mm}$ to introduce staggered hopping. The Hamiltonian of our 1D SSH model, accounting for the onsite perturbation, can be written as

$$\begin{aligned} H^x_{1D} = &\sum\nolimits_{i=1}^{N} [(c^{x\dagger}_{i,\alpha}c^x_{i,\alpha} + c^{x\dagger}_{i,\beta}c^x_{i,\beta})(f_0 + f_w^{\,1} + f_v^{\,1})] \\ &+ \sum\nolimits_{i=1}^{N} (wc^{x\dagger}_{i,\alpha}c^x_{i,\beta} + vc^{x\dagger}_{i,\beta}c^x_{i+1,\alpha} + \mathrm{H.c.}) \\ &- (c^{x\dagger}_{1,\alpha}c^x_{1,\alpha} + c^{x\dagger}_{N,\beta}c^x_{N,\beta})f_v^{\,1}, \end{aligned} \tag{4}$$

where i labels the dimerized unit cell; α and β each label a site within a unit cell; and w and v are the hopping of two nearest cavities, which are functions of ξ and η, respectively. $f_w^{\,1}$ and $f_v^{\,1}$ denote the onsite perturbation induced by one waveguide with side widths D_w and D_v, respectively.

In an ideal TBM, the SSH system has two boundary modes localized at two ends when $|w/v| < 1$. These two modes have zero energy, which is protected by the chiral symmetry $\sum_z = \sigma_z \oplus \sigma_z \oplus \ldots \oplus \sigma_z = \oplus_{i=1}^{N}\sigma_z$ [33]. In our case, Eq. (4) also has two boundary-mode solutions when $D_w < D_v$, as shown in Fig. 3(b). However, from the analysis above, chiral symmetry is preserved only near $\eta = 0.5$, where $f_v^{\,1} = 0$, at which the last term in Eq. (4) vanishes. Derivation of $\eta = 0.5$ significantly affects the frequencies of both bulk bands, whereas the size of the band gap is mostly unaffected. It also causes a small drift in the boundary mode frequencies. These are schematically shown in Fig. 3(a). The eigenvalues of Eq. (4) are plotted in Fig. 3(b) as functions of η. These outcomes can only be due to the perturbation of the onsite eigenfrequency, which agrees well with our theoretical model. To further validate these results, we use finite-element simulations to compute the eigenfrequencies of the CACS chain. The results are also shown in Fig. 3(b). Good agreement with our theory is seen.

IV. TWO-DIMENSIONAL ACOUSTIC SSH MODEL

We further extend our study to consider a 2D SSH model [34–37], which is a 2D square lattice with each unit cell having four coupled sites. The intracell and intercell hopping between two nearest sites are denoted as v and w, respectively. This model exhibits edge modes and second-order topological corner modes in the topologically nontrivial phase when $v > w$, which is characterized by a bulk topological invariant, i.e., nonzero quantized

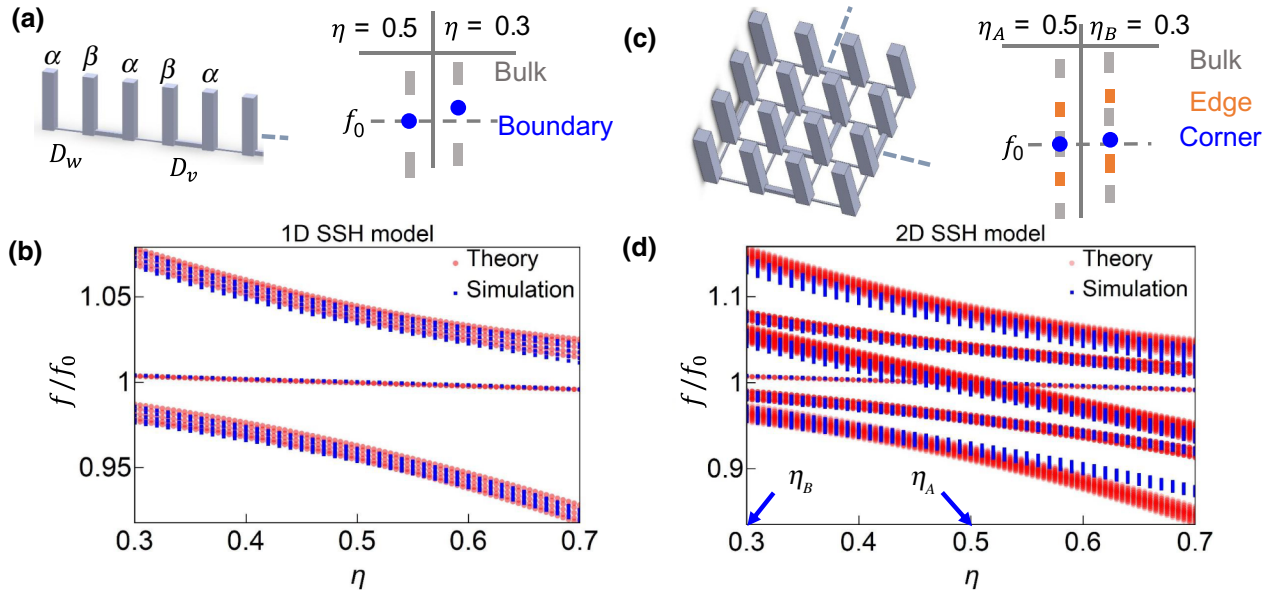

FIG. 3. (a) Schematic of 1D CACS chain, wherein the coupling waveguides have staggered widths $D_w = 3$mm and $D_v = 9$mm. System is an acoustic SSH model. Right panel schematically shows the boundary mode's position in the band gap is tunable by η. (b) Eigenspectrum of a 12-cavity acoustic SSH chain as functions of η with $L_0 = 120$mm (blue dots), with excellent agreement with the results from TBM theory (red dots). (c) Schematic of 2D CACS array, realizing a 2D SSH model. Position of the second-order topological corner modes is tunable by η. (d) Eigenspectra of a 12×12 CACS array, wherein blue (red) dots are the results from finite-element simulation (TBM theory).

polarizations. The Hamiltonian of a finite-sized 2D SSH lattice with $N \times N$ sites can be expressed as

$$H_{2D} + f_0 I_{N^2} = H_{1D}^{y} \otimes I_y + I_x \otimes H_{1D}^{x}, \tag{5}$$

where H_{1D}^{x} (H_{1D}^{y}) is the Hamiltonian of a 1D SSH chain along the x (y) direction, I_N (I_{N^2}) is an $N(N^2)$-dimensional identity matrix, $\otimes$ denotes the Kronecker product. Equation (5) implies that the eigenmodes of H_{2D} can be constructed from the eigenmodes in the 1D SSH model [38–40], as shown in Table I.

From Table I and the discussion of the 1D SSH model in Sec. III, it is straightforward to see that, when chiral symmetry exists in an ideal 2D SSH system, the four topological corner modes are degenerate at zero energy, which corresponds to f_0 in the acoustic model. (Here, we consider a sufficiently large lattice, so that the coupling among corner modes vanishes.) In Fig. 3(d), we plot the eigenvalues of H_{2D} as functions of η. The simulated results of a 2D acoustic SSH lattice are also shown together. It is seen that the corner modes are indeed at f_0 when $\eta = 0.5$, which is the point where the perturbation to onsite eigenfrequency by the waveguides vanishes. In other words, chiral symmetry exists for the 2D acoustic SSH lattice at $\eta = 0.5$.

On the other hand, by breaking the chiral symmetry, the relative spectral position of the bulk bands and the corner modes can be controlled by tuning η. For example, when η is near 0.5, the corner modes overlap with the middle bulk bands, thereby becoming bound modes in the continuum [41]. However, the corner modes can be found inside a band gap when chiral symmetry is broken, which is easily achieved by either reducing or increasing η [Fig. 3(d)].

TABLE I. Construction rules of the 2D SSH model from the 1D SSH model.

H_{1D}^{x} H_{1D}^{y}	Boundary mode $\phi_{1D}^{x,\,\text{boundary}}, f_{\text{boundary}}^{x}$	Bulk mode $\phi_{1D}^{x,\,\text{bulk}}, f_{\text{bulk}}^{x}$
Boundary mode $\phi_{1D}^{y,\,\text{boundary}}, f_{\text{boundary}}^{y}$	Corner modes: $\Phi_{2D}^{\text{corner}} = \phi_{1D}^{y,\text{boundary}} \otimes \phi_{1D}^{x,\text{boundary}}, f_{\text{boundary}}^{x} + f_{\text{boundary}}^{y} - f_0.$	Edge modes: $\Phi_{2D}^{\text{edge}} = \phi_{1D}^{y,\text{boundary}} \otimes \phi_{1D}^{x,\text{bulk}}, f_{\text{boundary}}^{y} + f_{\text{bulk}}^{x} - f_0.$
Bulk mode $\phi_{1D}^{y,\,\text{bulk}}, f_{\text{bulk}}^{y}$	Edge modes: $\Phi_{2D}^{\text{edge}} = \phi_{1D}^{y,\text{bulk}} \otimes \phi_{1D}^{x,\text{boundary}}, f_{\text{boundary}}^{x} + f_{\text{bulk}}^{y} - f_0$	Bulk modes: $\Phi_{2D}^{\text{bulk}} = \phi_{1D}^{y,\text{bulk}} \otimes \phi_{1D}^{x,\text{bulk}}, f_{\text{bulk}}^{x} + f_{\text{bulk}}^{y} - f_0$

V. EXPERIMENTAL VALIDATION

We experimentally demonstrate the two cases with $\eta_A = 0.5$ and $\eta_B = 0.3$, as shown in Fig. 3(c). The corresponding values of η are also marked in Fig. 3(d). The acoustic lattice is machined from a block of aluminum, as shown in Fig. 4(a). For the ease of fabrication, the cavities have a circular cross section with a radius $r = 12$ mm and a height of 120 mm. The distance between the two nearest cavities is $a = 40$ mm. The coupling waveguides have square cross sections with staggered lengths of $D_w = 3$ mm and $D_v = 9$ mm. A top plate covers and seals the lattice. There are opening ports on the top of each cavity, which are used for excitation and measurement. The coupling waveguides all have the same length L_t; η is, therefore, adjusted by tuning the cavity height L_0. This is achieved by injecting water to reduce the height of the cavities, since the impedance mismatch between water and air is huge. Adjusting the cavity height also shifts all onsite eigenfrequencies, f_0. However, such a shift does not affect the phenomena we aim to demonstrate.

We focus on two specific configurations. In configuration A, all cavities have a height of $L_A = 42$ mm. In configuration B, all cavities have a height of $L_B = 80$ mm. Comparing the eigenfrequencies of 2D SSH models and those obtained from simulations, we find that the two configurations correspond to $\eta_A \approx 0.48$ and $\eta_B \approx 0.27$, respectively, which are close to the values shown in Fig. 3(c). Therefore, we expect the corner mode to overlap with the bulk continuum for configuration A, and the corner mode to be in the band gap for configuration B, as shown in Fig. 3(d). We note that these values slightly differ from the ratios of the actual geometric parameters in the acoustic lattice. The discrepancies are attributed to two factors. First, the cavities all have curved sides, which affect the length of the coupling waveguides. Second, the depths of the coupling waveguides are not infinitesimal.

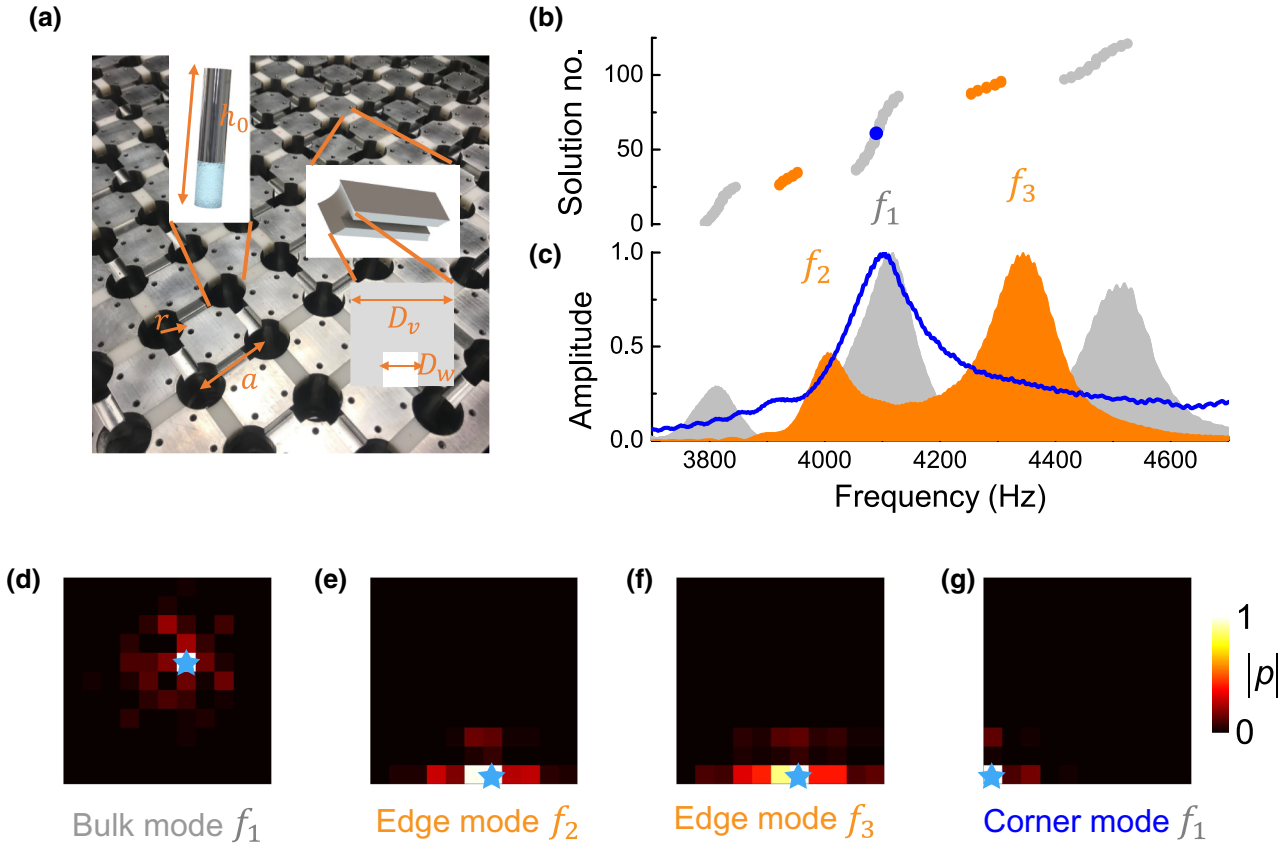

FIG. 4. (a) Photograph of a 2D CACS array with 11×11 cavities coupled by two types of coupling waveguides, one with a cross-section width of $D_v = 9$ mm, another has a side width $D_w = 3$ mm, as illustrated in the inset. (b) Eigenspectrum of configuration A with a cavity height $L_A = 42$ mm. Topological corner mode is marked by blue dots. Bulk modes and edge modes are plotted in gray and orange dots, respectively. Results show a largely symmetric distribution of eigenmodes near the frequency $f_{A0} = c/2L_A$, indicating the existence of chiral symmetry. (c) Measured pressure response spectra. Gray area represents bulk response, orange area represents edge response, and blue curve is the corner response. Pressure fields are measured when the system is excited by a source located at bulk (d); edge (e),(f); and corner (g), where blue stars indicate the respective source locations. Field distributions indicate bulk mode (d); edge modes (e),(f); and corner modes (g). Excitation frequency in (d) and (g) is the same, indicating the corner mode in (g) is a bound mode in the continuum.

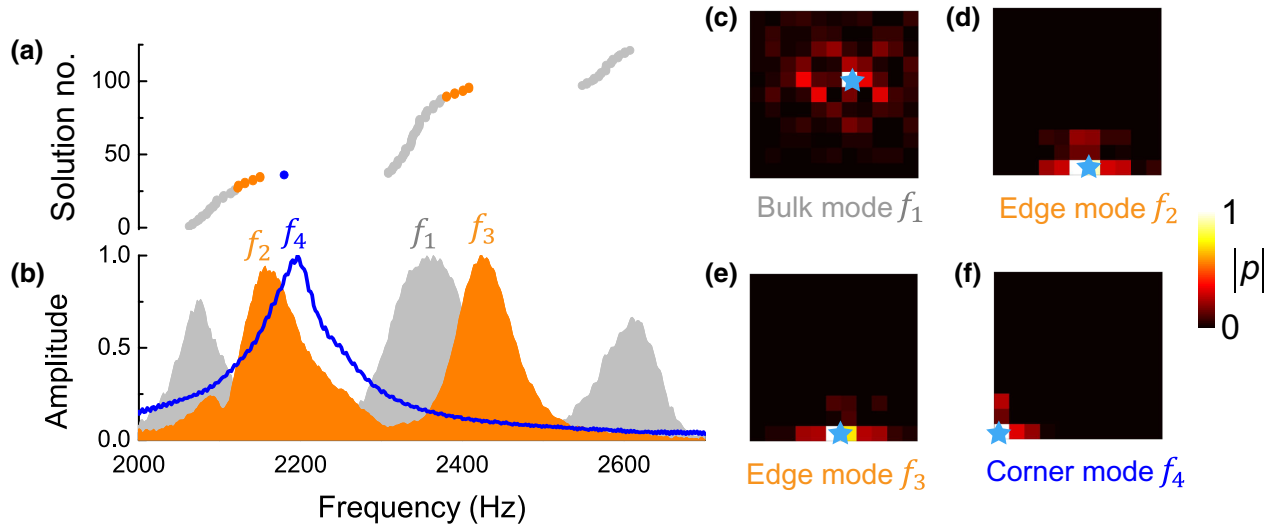

FIG. 5. (a) Simulated eigenspectrum of configuration B, with cavity height $L_B = 80$ mm. Topological corner modes (blue dots) are inside the first band gap. (b) Measured corner response (blue curve) has a peak localized in the bulk gap. Bulk (edge) response is the gray (orange) shading. Pressure field distributions of the bulk (c); edges (d),(e); and corner (f). Blue stars indicate the source locations.

The simulated eigenspectrum for configuration A is shown in Fig. 4(b). The edge modes appear in the gap, and the corner modes are found embedded in the second bulk band. Our measurement confirms our simulation results. First, we excite the system with a loudspeaker to excite the bulk. The measured response spectrum is shown in Fig. 4(c) with gray shading. Three separate regions of high-pressure responses are clearly observed. (It should be noted that we perform multiple measurements at different sites and select the result that best represents the bulk bands. A similar procedure was done for the edge-response measurements.) We further map out the distribution of the sound field in all cavities at 4101 Hz, as shown in Fig. 4(d), which clearly occupies the bulk. Next, we excite the system at the edge and measure the response spectra. Two peaks in the gap region are observed [orange in Fig. 4(c)]. The corresponding field maps are localized at the edge, indicating edge modes, as shown in Figs. 4(e) and 4(f). When excited at a corner, only one response peak is seen [blue in Fig. 4(b)]. The spatial map at the peak's frequency (4101 Hz) further confirms that the modes are strongly localized at the corner and decay rapidly into the bulk [Fig. 4(g)], which is characteristic of a corner mode. Since the corner modes and bulk modes share the same frequency, we reach the conclusion that the corner mode is a bound state in a continuum.

Next, the system is tuned to configuration B, with $\eta_B \approx 0.27$. The simulated eigenspectrum is plotted in Fig. 5(a), which shows that the corner modes are now located in the first band gap. This is consistent with our prediction, since chiral symmetry is broken for configuration B. In a similar manner, we experimentally obtain the bulk, edge, and corner response spectra [Fig. 5(b)] and the corresponding sound field distributions [Figs. 5(c)–5(f)]. The results confirm that the corner mode is indeed inside the first band gap.

The experimental results from the two configurations demonstrate that the spectral position of the corner modes, with respect to the bulk bands, is tunable by perturbation of the onsite eigenfrequency induced by chiral-symmetry breaking. These results also validate our analysis of TBM realized by the CACS.

VI. CONCLUSION

Here, we present a thorough study on the CACS, which is widely used as a platform to realize TBMs. We find that the length and number of coupling waveguides of a cavity not only tune hopping of the system, but also modulate the onsite eigenfrequency. The condition required for the onsite modulation to vanish is identified, which leads to a precise realization of the TBM in acoustics. Also, we show that the hopping sign is dependent on the length of the coupling waveguide. We apply our findings to the 1D acoustic SSH model and show that such modulation is equivalent to breaking the chiral symmetry. As a consequence, boundary modes with nonzero energy are found. By extending this to a 2D SSH model, we show that chiral-symmetry breaking can contribute as a degree of freedom for tuning the spectral location of second-order topological corner modes. We experimentally demonstrate such a capability by realizing a corner mode as a bound mode in the continuum and an in-gap corner mode.

Our work reveals multiple aspects of CACSs that have been largely ignored in previous studies. The results further cement CACSs as an important platform for the future

study of TBMs in acoustics, such as topological acoustics and non-Hermitian acoustics.

ACKNOWLEDGMENTS

This work is supported by the Hong Kong Research Grants Council (Grants No. GRF 12302420, No. 12300419, No. ECS 22302718, and No. CRF C6013-18G), the National Science Foundation of China Excellent Young Scientist Scheme (Hong Kong & Macau) (Grant No. 11922416) and Youth Program (Grant No. 11802256), and the Hong Kong Baptist University (Grants No. FRG2/17-18/056 and No. RC-SGT2/18-19/SCI/006).

[1] L. Lu, J. D. Joannopoulos, and M. Soljacic, Topological photonics, Nat. Photonics **8**, 821 (2014).
[2] T. Ozawa, H. M. Price, A. Amo, N. Goldman, M. Hafezi, L. Lu, M. C. Rechtsman, D. Schuster, J. Simon, and O. Zilberberg, Topological photonics, Rev. Mod. Phys. **91**, 015006 (2019).
[3] G. Ma, M. Xiao, and C. T. Chan, Topological phases in acoustic and mechanical systems, Nat. Rev. Phys. **1**, 281 (2019).
[4] R. Süsstrunk and S. D. Huber, Classification of topological phonons in linear mechanical metamaterials, Proc. Natl. Acad. Sci. **113**, E4767 (2016).
[5] Z. Yang, F. Gao, X. Shi, X. Lin, Z. Gao, Y. Chong, and B. Zhang, Topological Acoustics, Phys. Rev. Lett. **114**, 114301 (2015).
[6] X. Ni, C. He, X.-C. Sun, X.-P. Liu, M.-H. Lu, L. Feng, and Y.-F. Chen, Topologically protected one-way edge mode in networks of acoustic resonators with circulating air flow, New J. Phys. **17**, 053016 (2015).
[7] A. B. Khanikaev, R. Fleury, S. H. Mousavi, and A. Alu, Topologically robust sound propagation in an angular-momentum-biased graphene-like resonator lattice, Nat. Commun. **6**, 8260 (2015).
[8] Y. Ding, Y. Peng, Y. Zhu, X. Fan, J. Yang, B. Liang, X. Zhu, X. Wan, and J. Cheng, Experimental demonstration of acoustic chern insulators, Phys. Rev. Lett. **122**, 014302 (2019).
[9] J. Lu, C. Qiu, L. Ye, X. Fan, M. Ke, F. Zhang, and Z. Liu, Observation of topological valley transport of sound in sonic crystals, Nat. Phys. **13**, 369 (2017).
[10] C. He, X. Ni, H. Ge, X.-C. Sun, Y.-B. Chen, M.-H. Lu, X.-P. Liu, and Y.-F. Chen, Acoustic topological insulator and robust one-way sound transport, Nat. Phys. **12**, 1124 (2016).
[11] J. Mei, J. Wang, X. Zhang, S. Yu, Z. Wang, and M.-H. Lu, Robust and High-Capacity Phononic Communications Through Topological Edge States by Discrete Degree-of-Freedom Multiplexing, Phys. Rev. Appl. **12**, 054041 (2019).
[12] M. Xiao, W.-J. Chen, W.-Y. He, and C. T. Chan, Synthetic gauge flux and Weyl points in acoustic systems, Nat. Phys. **11**, 920 (2015).
[13] Z. Yang and B. Zhang, Acoustic Type-II Weyl Nodes From Stacking Dimerized Chains, Phys. Rev. Lett. **117**, 224301 (2016).
[14] X. Fan, C. Qiu, Y. Shen, H. He, M. Xiao, M. Ke, and Z. Liu, Probing Weyl Physics with One-Dimensional Sonic Crystals, Phys. Rev. Lett. **122**, 136802 (2019).
[15] W. A. Benalcazar, B. A. Bernevig, and T. L. Hughes, Quantized electric multipole insulators, Science **357**, 61 (2017).
[16] J. Langbehn, Y. Peng, L. Trifunovic, F. von Oppen, and P. W. Brouwer, Reflection-Symmetric Second-Order Topological Insulators and Superconductors, Phys. Rev. Lett. **119**, 246401 (2017).
[17] M. Ezawa, Higher-Order Topological Insulators and Semimetals on the Breathing Kagome and Pyrochlore Lattices, Phys. Rev. Lett. **120**, 026801 (2018).
[18] M. Serra-Garcia, V. Peri, R. Süsstrunk, O. R. Bilal, T. Larsen, L. G. Villanueva, and S. D. Huber, Observation of a phononic quadrupole topological insulator, Nature **555**, 342 (2018).
[19] K. Kawabata, K. Shiozaki, M. Ueda, and M. Sato, Symmetry and Topology in Non-Hermitian Physics, Phys. Rev. X **9**, 041015 (2019).
[20] R. El-Ganainy, K. G. Makris, M. Khajavikhan, Z. H. Musslimani, S. Rotter, and D. N. Christodoulides, Non-Hermitian physics and PT symmetry, Nat. Phys. **14**, 11 (2018).
[21] K. Ding, G. Ma, M. Xiao, Z. Q. Zhang, and C. T. Chan, Coalescence Emergence and Topological Properties of Multiple Exceptional Points and Their Experimental Realization, Phys. Rev. X **6**, 021007 (2016).
[22] Z.-G. Chen and Y. Wu, Tunable Topological Phononic Crystals, Phys. Rev. Appl. **5**, 054021 (2016).
[23] Y.-X. Xiao, G. Ma, Z.-Q. Zhang, and C. T. Chan, Topological Subspace-Induced Bound State in the Continuum, Phys. Rev. Lett. **118**, 166803 (2017).
[24] H. Xue, Y. Yang, F. Gao, Y. Chong, and B. Zhang, Acoustic higher-order topological insulator on a kagome lattice, Nat. Mater. **18**, 108 (2019).
[25] X. Ni, M. Weiner, A. Alù, and A. B. Khanikaev, Observation of higher-order topological acoustic states protected by generalized chiral symmetry, Nat. Mater. **18**, 113 (2019).
[26] X. Zhang, Z.-K. Lin, H.-X. Wang, Z. Xiong, Y. Tian, M.-H. Lu, Y.-F. Chen, and J.-H. Jiang, Symmetry-protected hierarchy of anomalous multipole topological band gaps in nonsymmorphic metacrystals, Nat. Commun. **11**, 65 (2020).
[27] F. Li, X. Huang, J. Lu, J. Ma, and Z. Liu, Weyl points and Fermi arcs in a chiral phononic crystal, Nat. Phys. **14**, 30 (2018).
[28] Y. Yang, H.-X. Sun, J.-P. Xia, H. Xue, Z. Gao, Y. Ge, D. Jia, S.-Q. Yuan, Y. Chong, and B. Zhang, Topological triply degenerate point with double Fermi arcs, Nat. Phys. **15**, 645 (2019).
[29] Z. Zhu, X. Huang, J. Lu, M. Yan, F. Li, W. Deng, and Z. Liu, Negative Refraction and Partition in Acoustic Valley Materials of a Square Lattice, Phys. Rev. Appl. **12**, 024007 (2019).
[30] P. Gao, Z. Zhang, and J. Christensen, Sonic valley-Chern insulators, Phys. Rev. B **101**, 020301 (2020).

[31] C. W. Peterson, W. A. Benalcazar, T. L. Hughes, and G. Bahl, A quantized microwave quadrupole insulator with topologically protected corner states, Nature **555**, 346 (2018).
[32] H. Xue, Y. Ge, H.-X. Sun, Q. Wang, D. Jia, Y.-J. Guan, S.-Q. Yuan, Y. Chong, and B. Zhang, Quantized octupole acoustic topological insulator, arXiv 1911.06068 (2019).
[33] M. Koshino, T. Morimoto, and M. Sato, Topological zero modes and Dirac points protected by spatial symmetry and chiral symmetry, Phys. Rev. B **90**, 115207 (2014).
[34] F. Liu and K. Wakabayashi, Novel Topological Phase with a Zero Berry Curvature, Phys. Rev. Lett. **118**, 076803 (2017).
[35] Z.-G. Chen, C. Xu, R. Al Jahdali, J. Mei, and Y. Wu, Corner states in a second-order acoustic topological insulator as bound states in the continuum, Phys. Rev. B **100**, 075120 (2019).
[36] L.-Y. Zheng, V. Achilleos, O. Richoux, G. Theocharis, and V. Pagneux, Observation of Edge Waves in a Two-Dimensional Su-Schrieffer-Heeger Acoustic Network, Phys. Rev. Appl. **12**, 034014 (2019).
[37] Z. Zhang, M. Rosendo López, Y. Cheng, X. Liu, and J. Christensen, Non-Hermitian Sonic Second-Order Topological Insulator, Phys. Rev. Lett. **122**, 195501 (2019).
[38] M. Lohse, C. Schweizer, H. M. Price, O. Zilberberg, and I. Bloch, Exploring 4D quantum Hall physics with a 2D topological charge pump, Nature **553**, 55 (2018).
[39] Z.-G. Chen, W. Zhu, Y. Tan, L. Wang, and G. Ma, arxiv 1912.10267 (2019).
[40] W. Zhu and G. Ma, Distinguishing topological corner modes in higher-order topological insulators of finite size, Phys. Rev. B **101**, 161301(R) (2020).
[41] C. W. Hsu, B. Zhen, A. D. Stone, J. D. Joannopoulos, and M. Soljačić, Bound states in the continuum, Nat. Rev. Mater. **1**, 16048 (2016).